Check for updates

Advanced Materials

ADVANCED MATERIALS
www.advmat.de

RESEARCH ARTICLE

Each Grain Different in Its Own Way: Size-Dependent Pseudosymmetry in Fivefold Twinned Nanoparticles Mapped by 4D-STEM

Oliver Lin[1] | Zhiheng Lyu[2] | Hsu-Chih Ni[2] | Xiaokang Wang[2] | Yetong Jia[3] | Chu-Yun Hwang[2] | Lehan Yao[2] | Sohini Mandal[1] | Jian-Min Zuo[2,4,5] | Qian Chen[1,2,4,6,7]

[1]Department of Chemistry, University of Illinois, Urbana, Illinois, USA | [2]Department of Materials Science and Engineering, Grainger College of Engineering, University of Illinois, Urbana, Illinois, USA | [3]School of Mechanical Engineering, Purdue University, West Lafayette, Indiana, USA | [4]Materials Research Laboratory, University of Illinois, Urbana, Illinois, USA | [5]Monash Centre for Electron Microscopy, Monash University, Clayton, VIC, Australia | [6]Department of Chemical and Biomolecular Engineering, University of Illinois, Urbana, Illinois, USA | [7]Beckman Institute for Advanced Science and Technology, University of Illinois, Urbana, Illinois, USA

Correspondence: Qian Chen (qchen20@illinois.edu)

Received: 2 November 2025 | **Revised:** 1 April 2026 | **Accepted:** 2 April 2026

Keywords: 4D-STEM strain mapping | decahedral nanoparticles | fivefold twinned nanostructure | geometric frustration | size-dependent pseudosymmetry

ABSTRACT

Geometric frustration arises when geometry prevents the simultaneous satisfaction of local interactions, producing pseudosymmetry and emergent behaviors. Pseudosymmetric features in crystalline nanomaterials are known to appear as local strain and distortion, but how these features depend on particle size and govern structural stability remains unclear. Here we present the first study of a particle size-dependent crossover in pseudosymmetry of multi-twinned gold nanoparticles (NPs) by nanoscale strain mapping based on 4D scanning transmission electron microscopy. Analysis of 26 decahedral NPs (edge length: 20–55 nm) reveals the manifestation of pronounced heterogeneity in multiple modes of in-plane strain and displacement field in small NPs, caused by geometric gap closing of the five tetrahedral grains. As particle size increases, the strain fields in NPs homogenize across grains and local phases shift from predominantly lower-symmetry body-centered tetragonal to face-centered cubic character, approaching bulk gold. We identify a crossover particle size of ~35 nm, well below the bulk, which is also correlated to a transition from modified-Wulff particles to pentagonal bipyramids, consistent with finite element predictions. The particle size-dependent strain and pseudosymmetry at the nanoscale can extend to other geometrically frustrated nanostructures, guiding design and control of crystalline solids and phase transformation for catalysis, photonics, electronics, and energy storage.

1 | Introduction

Geometric frustration occurs when the system's geometry precludes the simultaneous satisfaction of all local interactions, producing complex structures and properties such as chirality for polarization sensitive imaging, spin ice states in ferromagnetic Kagome lattices for quantum computing, and origami-inspired surface with adjustable compressibility as robotics [1, 2]. In crystalline systems, accommodation of geometric frustration can induce slight distortion from ideal lattices and lead to *pseudosymmetry*, a phenomenon recognized decades ago as an evolutionary adaptation in biological structures [3, 4]. For instance, the neuraminidase of the influenza virus exhibits sliding domains that generate pseudosymmetry. The resulted structural flexibility

© 2026 Wiley-VCH GmbH

is capable of surpassing the limitations of the lock-and-key mechanism to more effectively evade host's immune system [5].

Pseudosymmetry also exists in synthetic nanomaterials, though it has been much less discussed [6]. For example, geometrically frustrated fivefold twinned decahedral (Dh) nanoparticles (NPs) serve as the cornerstone for the synthesis of a wide range of shape-controlled NPs, such as rods, wires, and bipyramids of gold, silver, and copper [7–9]. These NPs exhibit remarkable catalytic, plasmonic, mechanical, and chiroptical properties for applications in optoelectronics, bioimaging and biosensing, fuel cells, and machine vision [10–13]. Pseudosymmetry emerges in these fivefold twinned NPs because fivefold rotational symmetry is crystallographically forbidden in 3D; imposing the fivefold rotational symmetry onto face-centered cubic (*fcc)* lattice causes atomic displacements in the NPs, altering the local lattice symmetry, strain, and properties of NPs [14–17]. As a prominent example of "strain engineering," unrelaxed strains at the twin boundaries of fivefold twinned NP catalysts can modulate the energy of *d*-band electrons and substantially enhance the catalytic activity and selectivity [18]. However, understandings of the structural distortion and pseudosymmetry at the nanoscale remains very limited. For fivefold twinned NPs [14, 19], early studies suggested that geometric frustration is stabilized by forming low energy {111} facets to minimize surface energy and accommodate the energetic cost of bulk strain and twinning [20]. Continuum models further showed that surface energy and strain energy scale to r^2 and r^3, respectively, where r is the particle radius assuming a spherical shape [20], complicating the square–cube law that NPs inherently follow [21]. This difference in scaling law suggests a particle size-dependent pseudosymmetry behavior, which remains unexplored experimentally. Detailed modeling of the structural distortion of NPs and its impact on properties is challenging [22] because colloidally-synthesized fivefold twinned NPs are complex, with variations in particle size (from a few nanometers (nm) to hundreds of nm), shape (from perfect decahedra, truncated Marks decahedra, to pentagonal rods) [23, 24], composition, defect, and facet-dependent ligand adsorption. Previous experimental studies focused on NPs of edge length (d) smaller than 10 nm, a size range that allows direct imaging of atoms or lattice fringes by scanning/transmission electron microscopy (S/TEM) [25]. Yet many geometrically frustrated NPs are larger and contain phase complexity [26, 27] (comprehensive literature survey in Note S1). There remains extensive interest in understanding how these particles sustain and stabilize the structure against strain energy and twinning across a wide particle size range.

Here we present a *particle size-dependent* crossover of pseudosymmetry behaviors in fivefold twinned gold Dh NPs, from a total of 26 particles (Experimental Section) with large edge length d ranging from 20 to 55 nm. We develop a workflow integrating 4D scanning transmission electron microscopy (4D-STEM) [28] capable of imaging nanoscopic strain with diffraction pattern (DP) analysis following the principles of solid mechanics and crystallography, to map the local strain, lattice displacement, and symmetry of NPs at the otherwise inaccessible nm spatial mapping resolution. Ideal gold Dh NP shapes have a D_{5h} point group and accommodate five tetrahedral grains around a shared axis, resulting in an angular geometric misfit known as a disclination of 7.35°. By analyzing the DPs from 4D-STEM (Figure 1a), we map the in-plane strain field (ε_{220}, $\varepsilon_{002,}$ and shear strain, γ) and rigid body rotation (R) of local lattices in each grain while considering the full complexity of the fivefold twin. Solid mechanics principles allow us to merge the five grains to a global coordinate and relate the strain map to lattice displacements derived from 4D-STEM. The whole-particle strain and displacement maps show that all our NPs, regardless of size, are strained heterogeneously at the nm scale, remarkably maintaining normal strains averaged to 2% in magnitude without forming extended defects like dislocations or nanotwins. The NPs exhibit size-independent spatial patterns of γ and R to close the 7.35° geometric gap. Meanwhile, size-dependent behaviors emerge. Large Dh NPs ($d > 35$ nm) exhibit faceted pentagonal edges and the "bulk" behavior, where ε_{220} and ε_{002} show clear *intra-grain* heterogeneity, with strain concentrated at particle edges, and minor *inter-grain* heterogeneity. Both features are consistent with a finite element analysis (FEA) modeling of a bulk perfect decahedron. In contrast, for small NPs ($d < 35$ nm), ε_{220} and ε_{002} are uniform in each grain, but show large inter-grain heterogeneity, revealing a "nanosize" effect that we attribute to early-stage grain merging pathways during NP synthesis, an effect not captured in previous strain field models [29]. This crossover from nano to bulk behaviors at $d \sim 35$ nm, well below a true bulk size, correlates to pseudosymmetry, which we define and measure from the crystal structure of Au. While the NP lattice symmetry is predominantly body-centered tetragonal (*bct*) lattice expected for fivefold twinned NPs [17], we observe an intriguing emergence and spatial redistribution of regions of bulk *fcc* lattice as the particle size increases, to restore the ideal symmetry under strain.

Our focus on this particular size range NPs (20–55 nm) builds on the enormous application opportunities of these NPs as they offer advantageous performance across catalysis, plasmonics, and batteries: in catalysis, they balance activity, selectivity, and stability by maintaining high surface area while avoiding dissolution/Ostwald ripening often seen in <10 nm particles, and their favorable fraction of low-coordinated sites can suppress side reactions. For example, for CO_2 electroreduction, 44-nm Cu nanocubes show maximal ethylene selectivity, whereas < 20 nm particles favor hydrogen evolution, and surface twin boundaries further enhance CO binding and C2+ selectivity [30–32]. In plasmonics, Au NPs in this size range exhibit stronger localized surface plasmon resonance due to larger volume and sharper tips than smaller NPs, enabling enhanced dipolar and higher-order modes as well as better longitudinal/transverse mode separation [33–35]. NPs of around 50 nm in size often optimize surface-enhanced Raman scattering by balancing field enhancement and absorption [36–38]. For battery electrodes, particles of these sizes undergo solid solution-like rather than two-phase transitions, accelerating ion intercalation and boosting capacity versus microparticles [28, 39–42].

Our work on fivefold twinned NPs of a wide size range elucidates how the internal pseudosymmetric distortion embeds in nanoscale heterogeneity and exhibits clear size-dependence with an early crossover to bulk behaviors. As geometric frustration has been found beyond *fcc* noble metals, such as intermetallics of AuCu and FePt in face-centered tetragonal structure with disclination [43–45], our understanding can extend to these other phases and strain engineered NP-based functional

15214095, 0, Downloaded from https://advanced.onlinelibrary.wiley.com/doi/10.1002/adma.202521658 by University Of Illinois At Urba, Wiley Online Library on [16/04/2026]. See the Terms and Conditions (https://onlinelibrary.wiley.com/terms-and-conditions) on Wiley Online Library for rules of use; OA articles are governed by the applicable Creative Commons License

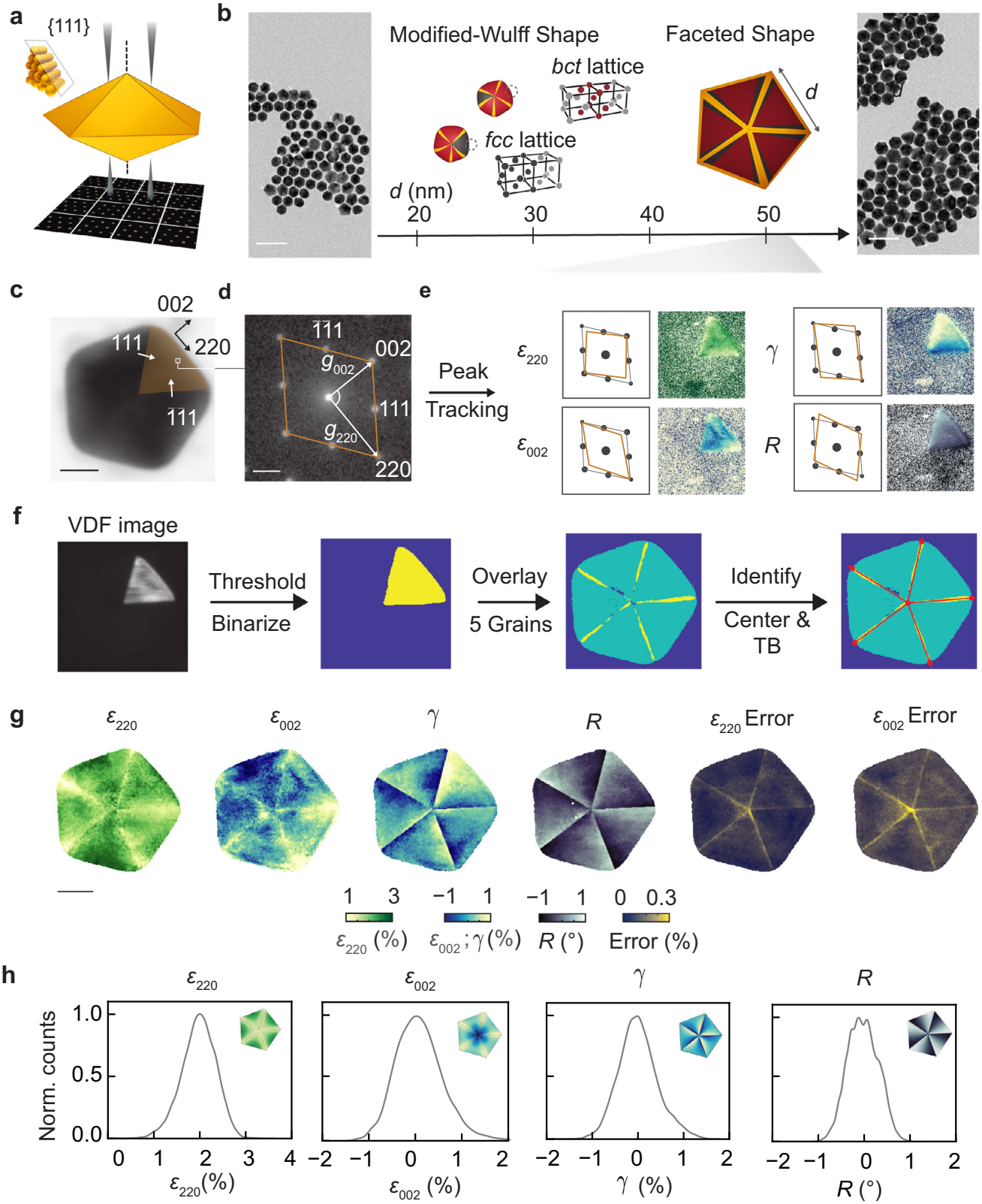

FIGURE 1 | Mapping of heterogeneous strain distributions in colloidally synthesized Au Dh NPs by 4D-STEM. (a) Schematics of a 4D-STEM measurement configuration that aligns the incident electron beam to the disclination axis of a gold Dh NP. (b) TEM images (left: d = 20–30 nm, right: d = 40–55 nm) and illustration of how the particle shape and symmetry of Au Dh NPs change as the edge length d increases from 20 to 55 nm. (c) Virtual bright field (VBF) of a particle of d = 50.1 nm, with a grain highlighted to show its local lattice coordinate. (d) DP of the pixel boxed in (c), labeled with the index of each diffraction disc, as well as the g-vectors and angle in between. (e) The types of lattice distortion modes can be identified by measuring the positions of diffraction discs, including normal strain in (220) and (002) directions (ε_{220}, ε_{002}), shear strain (γ), and lattice rotation (R). On the right are the corresponding mapping results of the highlighted grain. The color ranges follow the color bars defined in (g). (f) Data processing workflow using virtual

15214095, 0, Downloaded from https://advanced.onlinelibrary.wiley.com/doi/10.1002/adma.202521658 by University Of Illinois At Urba, Wiley Online Library on [16/04/2026]. See the Terms and Conditions (https://onlinelibrary.wiley.com/terms-and-conditions) on Wiley Online Library for rules of use; OA articles are governed by the applicable Creative Commons License

materials. Our 4D-STEM-based local strain, lattice displacement, and symmetry mapping can also help broadly the understanding of twin boundary formation, strain relaxation, and phase transformation in other materials used as catalysis, mechanical absorptive materials, electronic devices, and energy storage materials.

2 | Results

2.1 | 4D-STEM Mapping of Strain Tensor Components in Gold Dh NPs

Gold Dh NPs are colloidally synthesized using seed-mediated growth [9], where the NP sizes are controlled by the seed amount (Experimental Section, Figure 1b; Figure S1). All the Dh NPs maintain fivefold twins over the size range of $d = 20$ to 55 nm. Closing the geometric gap requires lattice straining and structural distortion. As such, we expect to observe predominately *bct* lattice, along with the redistribution of local *fcc* lattice throughout the NPs (Figure 1b). We observe mostly ideal {111} facets in the NPs without further faceting, unlike the Marks Dh more commonly observed in large Pd NPs [46]. The NPs transition from decahedron of highly rounded corners (i.e., modified Wulff shape) to sharp-cornered pentagonal bipyramidal shape as their sizes increase (Note S2 and Figure S2) [47].

To map the in-plane components of strain tensors, 4D-STEM is used to collect DPs at a 1.7 nm electron probe size, 0.376 nm step size, and a convergence angle of 0.6 mrad (Experimental Section). The partial overlapping of sampling regions between neighboring steps is performed intentionally to ensure continuity for displacement field mapping. We align the particle to the disclination axis, so that all the tetrahedral grains are along the [110] axis. Figure 1c shows a typical virtual bright field (VBF) image of a large particle ($d = 50.1$ nm). As the five grains are positioned in fivefold rotational symmetry, the crystallographic direction in each grain is rotated relatively in-plane. The (220) and (002) lattice planes, which are parallel and perpendicular to the grain edge, respectively (Figure 1c), are the orthogonal basis that define the local coordinate for strain mapping. Using the DP (Figure 1d) at one pixel of VBF (labeled in Figure 1c) as an example, strain mapping tracks the Bragg peak positions of available diffraction discs by the circular Hough transform method [48], fits a local lattice, and then compares with a global reference lattice of bulk gold (Note S3). The normal strains (ε_{220} and ε_{002}) measured based on the lengths of g-vectors (g_{220} and g_{002}), the shear strain (γ, change of the angle between the g-vectors relative to the angle for an ideal *fcc* lattice), and the in-plane rotation (R) are extracted from the DPs at each pixel, corresponding to different distortion modes in reference to an ideal lattice (Figure 1e). Because each grain has a different local coordinate, the strain analysis is performed five times correspondingly, masked and combined to generate the strain maps at the whole-particle level with all four components resolved (Figure 1f; Figures S3 and S4).

The whole-particle maps of the in-plane strain components (Figure 1g) reveal nanoscopic heterogeneity. In the example of the large particle ($d = 50.1$ nm), the ε_{220} map shows that the (220) lattice plane is all in tension, more at the particle edge (averaged at 2%) than at the twin boundary. In comparison, for ε_{002} along (002) lattice plane, compressive strain occurs at particle edges (−1%) with tensile strain at the twin boundary (1%). Both γ and R maps show alternating patterns within each grain over the range of −1% to 1% and −1° to 1°, respectively, with the extrema occurring near twin boundaries. Figure 1h lists the histograms of the four strain components.

FEA simulations of the same set of strain tensor components of a perfectly shaped Au decahedron (insets in Figure 1h) have patterns matching qualitatively with our $d = 50.1$ nm particle, although the latter shows more heterogeneity, suggesting that the projected volumetric strain field of the large particle can be modeled using bulk anisotropic elasticity to close the 7.35° gap. FEA models the 3D particle shape with the strain tensor components projected and averaged along the same direction as in our experiment for comparison (Note S4 and Figure S5).

The 4D-STEM-based strain mapping provides comprehensive measurements of local strain and lattice distortion at the nm spatial resolution, in principle applicable to samples of thickness up to ~300 nm [28, 49–52]. The convergence of all five grains using one global reference reveals the nanoscale heterogeneity and the long-range effect of lattice straining across grains. In comparison, previous studies of small Dh NPs ($d < 10$ nm) used aberration-corrected TEM imaging to apply geometric phase analysis (GPA) to high-quality electron microscopy images, obtaining γ and R of the same alternating patterns that we observe to explain gap closing but not the other components [53]. The alternating patterns were attributed to the nature of the structural distortion based on disclination. We show that the same mechanism applies to large NPs. In the more recent study using atom electron tomography for Dh NPs of $d \sim 5$ nm, the 3D atomic coordinates of NPs were directly used to calculate ε_{220} in one grain, showing tensile strain at the edge [54], consistent with Figure 1g, but not for the complete mapping of all five grains to observe intra- or inter-grain heterogeneity.

2.2 | Visualization of Geometric Gap Closing via Heterogeneous Straining and Lattice Displacement

To visualize lattice distortions in real space that close the geometric gap, Figure 2a summarizes the symbolic representations of distortion modes. Here we denote a reference *fcc* lattice (undistorted bulk gold) viewed from [110] direction as a perfect rectangle. At the center of the particle edge, there are minimal

dark field (VDF) images to identify particle center and five twin boundaries. "TB" means twin boundary, following the details in Note S3 and Figure S3. (g) Experimental strain maps and the associated strain error of the Au Dh NP in (c). (h) Histograms of strain values normalized to the maximum of each component from experimental maps. Insets: FEA simulated strain field components. Each map has the color bar spanning to the same range as the corresponding experimental map. Scale bars: images (b): 100 nm; (c,g): 20 nm; DP in (d): 5 nm^{-1}.

15214095, 0, Downloaded from https://advanced.onlinelibrary.wiley.com/doi/10.1002/adma.202521658 by University Of Illinois At Urba, Wiley Online Library on [16/04/2026]. See the Terms and Conditions (https://onlinelibrary.wiley.com/terms-and-conditions) on Wiley Online Library for rules of use; OA articles are governed by the applicable Creative Commons License

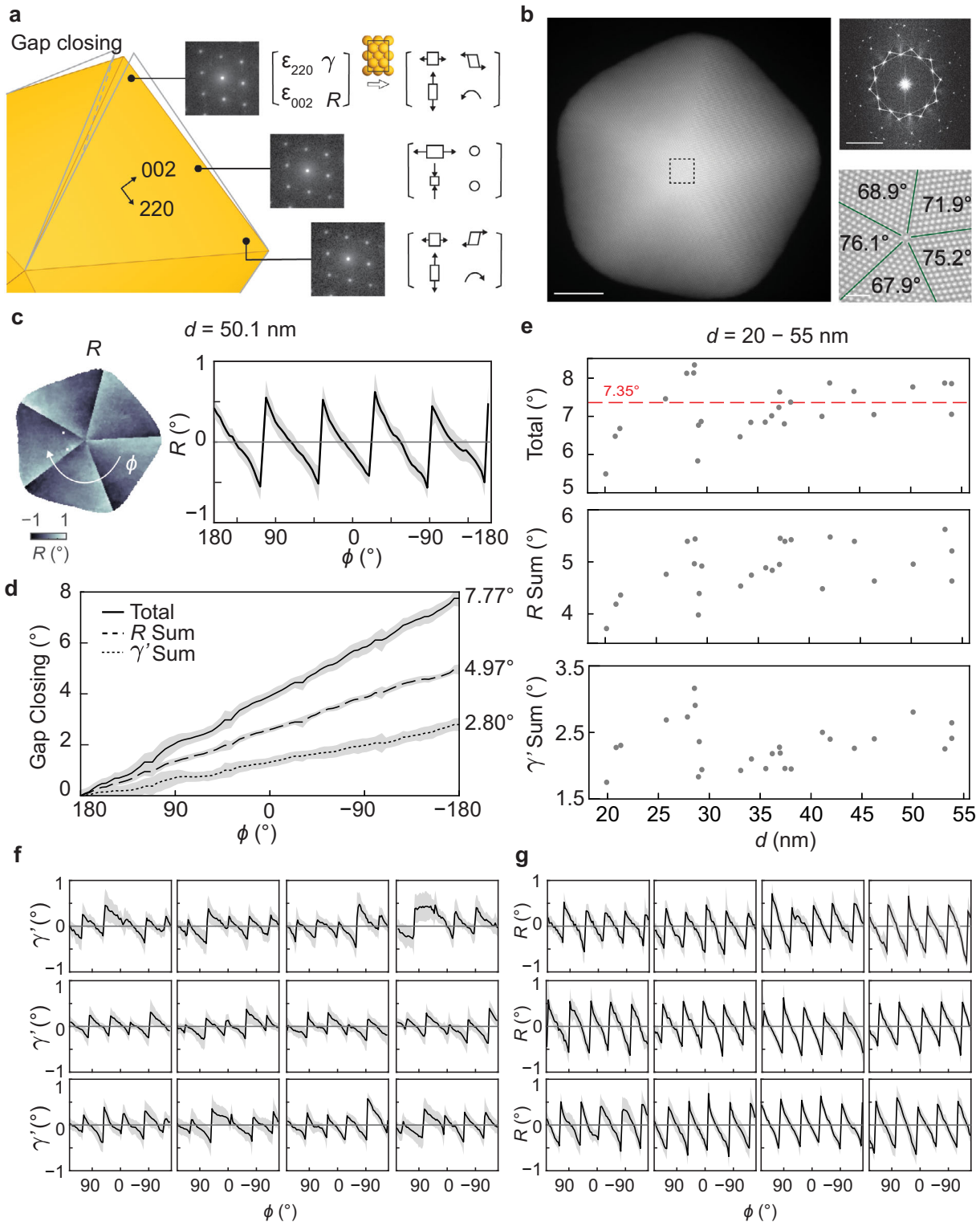

FIGURE 2 | Geometric gap closing and heterogeneity. (a) Schematic of spatially varying lattice distortion in different modes to close the geometric gap imposed by the fivefold twin structure, using the DPs of different parts of the NP shown in Figure 1c–g ($d = 50.1$ nm) as an example. (b) Aberration-corrected HAADF STEM image (left) of a particle of $d = 36.2$ nm with its fast Fourier transform (FFT, right top). Figure S6 shows the lack of large-scale defects. The zoom-in STEM image (right bottom) at the disclination axis shows the uneven distribution of angles divided by the five grains. (c) The radial averaging of the alternating patterns of R of $d = 50.1$ nm is plotted over the azimuthal angle (ϕ) and summed to compute the values in (d) and the shaded areas are the standard deviation. (d) The sum of R and γ' to quantify the angular distortion to close the geometry gap. Here γ' of a unit of degree (°) is converted from γ (dimensionless), following details noted in Note S5. (e) Scattered plots of all the summed values over the 26 particles studied in this work of different particle sizes. (f, g) The radial averaging profiles of γ' (f) and R (g) with increasing d between 20 and 55 nm arranged from left to right and top to down. Note γ' are heterogeneous for all particles while R trends toward homogeneous with increasing size. Scale bars in (b): HAADF overview image: 20 nm; FFT image: 5 nm^{-1}; zoom-in image: 1 nm.

15214095, 0, Downloaded from https://advanced.onlinelibrary.wiley.com/doi/10.1002/adma.202521658 by University Of Illinois At Urba, Wiley Online Library on [16/04/2026]. See the Terms and Conditions (https://onlinelibrary.wiley.com/terms-and-conditions) on Wiley Online Library for rules of use; OA articles are governed by the applicable Creative Commons License

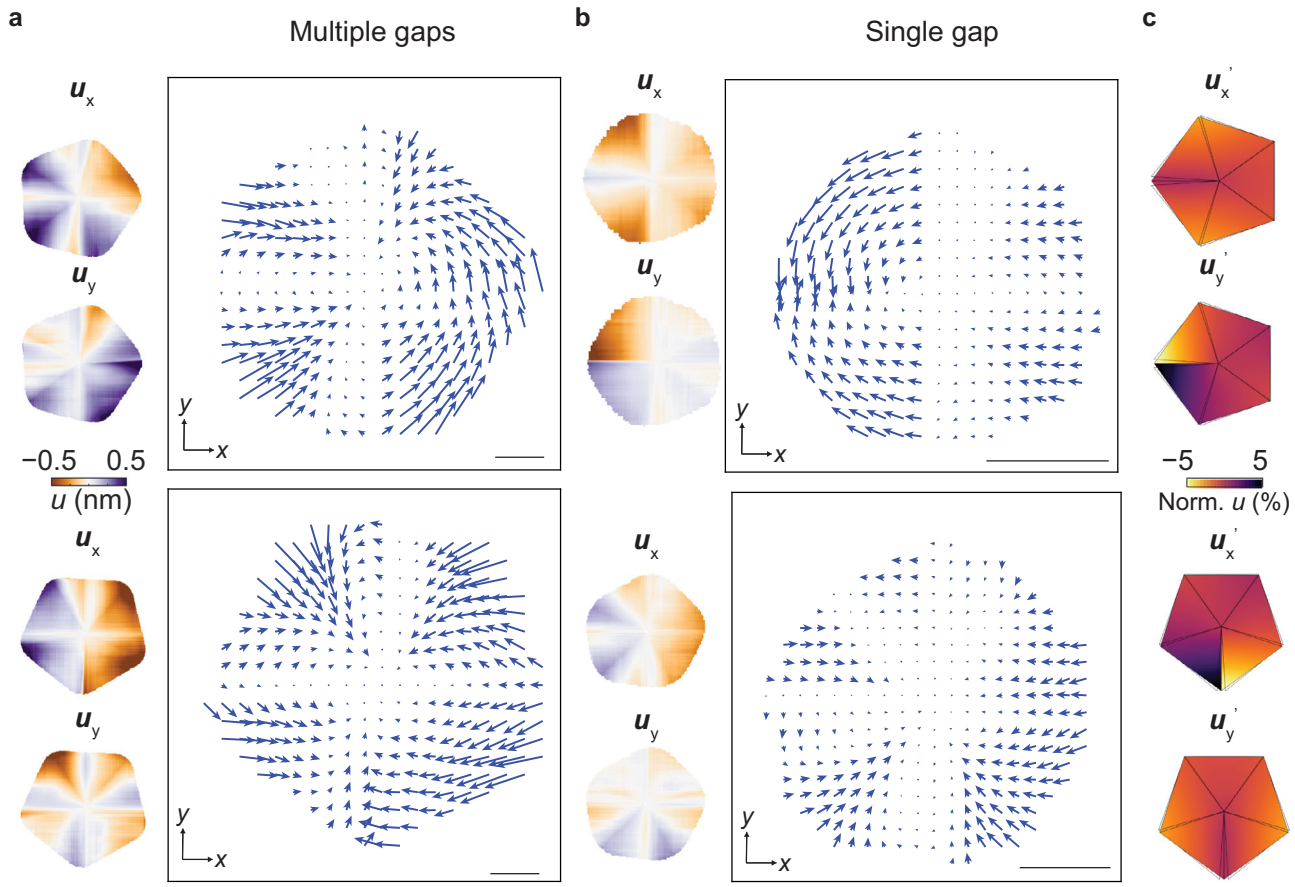

FIGURE 3 | The displacement field maps in the global Cartesian coordinate system. (a) The experimental displacement vector field maps (right) and magnitude maps of each direction (left) of two representative large particles, $d = 50.1$ nm (top) and $d = 54.0$ nm (bottom), showing features of closing multiple gaps. (b) The experimental displacement vector field maps (right) and magnitude maps of each direction (left) of two representative small particles, $d = 20.5$ nm (top) and $d = 27.2$ nm (bottom), showing features of closing a single gap. (c) Simulated displacement field magnitude map ($\boldsymbol{u}_x$' and $\boldsymbol{u}_y$') of particles closing a single gap, with their gaps pointing to the left (top) and downward (bottom). The simulated value of the displacement is normalized to the edge length of the particle model. Scale bars: 10 nm.

γ and R, or lattice shear and rotation (both denoted by °), but large ε_{220} as tensile strain and ε_{002} as compressive strain (distorted rectangles). Near the particle twin boundaries, ε_{220} is reduced, and ε_{002} turns tensile, with severe angular distortion visible in γ and R, denoted as a sheared rhomboid. At the two twin boundaries of one grain, the directions of the angular distortion are opposite, as if the grain is bent.

High-magnification high-angle annular dark-field (HAADF) STEM images (Figure 2b) show that the five grains partition the full 360° unevenly, suggesting the importance to analyze the entire NP with each grain resolved individually first and then connected. GPA analysis of the HAADF images (Figure S6), as a comparison with 4D-STEM analysis, yields poor quantitative strain maps due to insufficient image quality caused by the large NP thickness.

The accumulated lattice distortion in terms of angles to close the gap is calculated from the γ and R maps. Using the particle in Figure 1c–g as an example, because the lattice rotation features mostly vary not radially but azimuthally, the values of R can be averaged along the radial direction to collapse the 2D map (Figure 1g) into a plot (Figure 2c) along the azimuthal angle (ϕ) from −180° to 180°. R values exhibit an alternating pattern, smoothly varying within a grain, and have sharp transitions across twin boundaries. The maximum R varies across the grains. To calculate the angular lattice distortion for the entire particle, the same plotting is applied to γ', namely γ converted to degree values (Note S5), and the amount of distortion inside each grain is summed (Figure 2d). This workflow is applied to the 26 differently sized NPs (Figure 2e–g; Figure S7). The statistics of this large number of NPs show a plateau around the theoretically expected value of 7.35° when $d > 35$ nm (Figure 2e). When $d < 35$ nm, the total sums fluctuate around 7.35° mostly by ~1°, suggesting that gap closing via lattice shearing and rotation still works, although the radially averaged angular distortions might not be the most accurate due to more heterogeneity in small NPs.

While γ and R maps capture the angular distortion of each grain using the local coordinate, the 2D displacement field maps offer a holistic visualization of lattice rearrangement for the entire particle, for the first time using DPs. In our 4D-STEM experiment, the pixel size in a strain map is known and small (0.376 nm). The strain tensor map is used to derive a displacement field map, although these two are distinct and not necessarily spatially correlated (Note S6), where the displacement field map shows

15214095, 0, Downloaded from https://advanced.onlinelibrary.wiley.com/doi/10.1002/adma.202521658 by University Of Illinois At Urba, Wiley Online Library on [16/04/2026]. See the Terms and Conditions (https://onlinelibrary.wiley.com/terms-and-conditions) on Wiley Online Library for rules of use; OA articles are governed by the applicable Creative Commons License

how each pixel (not an atom) of a "hypothetical" continuous solid moves to close the geometric gap. Because Dh NPs are oriented to have mirror symmetry on the *x*-*y* plane during DP collection, we assume that the 2D displacement map is representative of lattice rearrangement of the entire NP. By fixing the center of a NP as zero displacement, we plot the 2D displacement field maps as a vector of two components of $\boldsymbol{u}_x$ and $\boldsymbol{u}_y$ along the global *x* and *y* axes (Figure 3a,b). For the small NPs (d = 20.5 nm and 27.2 nm, Figure 3b), one single geometric gap closure is shown at the twin boundary at the left side and the bottom of the particles, respectively, where the grains adjacent to the twin boundary move toward it. Similar features of $\boldsymbol{u}_x$ and $\boldsymbol{u}_y$ can be reproduced in FEA simulation when modeling the closure of one geometric gap (Figure 3c). In contrast, the large NPs (d = 50.1 nm and 54.0 nm, Figure 3a) show closure of multiple distributed gaps. The common observation that the closure of gaps is not uniformly distributed among all grains can be originated from the various pathways of forming fivefold twins during colloidal synthesis, such as successive twining and layer-by-layer growth [55], leading to grain-to-grain variation.

Such visualization of displacement fields is made possible by compiling the displacement vectors from the particle center over all five grains with the same reference and coordinate. The maps consider the in-plane strain components in a global 2D coordinate system, not by tracking atomic columns, which are inaccessible in large NPs, in spirit aligned with the particle image velocimetry analysis in optical microscopy used to map the collective motions of colloids without localizing each of them [56].

2.3 | Particle Size-Dependent Strain Distribution: Intra- and Inter-Grain Heterogeneity

The spatial distributions of lattice distortion exhibit a nano to bulk crossover when we extend the strain mapping analysis to Dh NPs of different sizes. Figure 4a shows the HAADF images and the maps of all strain components and rotation (ε_{220}, ε_{002}, γ, and R) of Dh NPs with d varying from 20 to 55 nm. As shown in Figures 2e–g and 4a and Figure S7, the alternating patterns in γ' and R maps across five grains sustain for all the NPs, confirming the size-*in*dependent nature of the gap closing mechanism as discussed earlier. Yet, the maps of normal strain components (ε_{220} and ε_{002}) show a clear NP size dependence. As noted in Figure 2e, d = 35 nm roughly separates the two size regions of NP behaviors in total misfit angles. Here, as a nice coincidence, around d = 35 nm also defines the size regions for normal strain components. For small particles (d < 35 nm), the ε_{220} or ε_{002} distribution in each grain shows more of a diffusive feature, meaning each grain is homogeneously strained, yet the values of strain can be different among grains. The particles have significant *inter*-grain heterogeneity with minor *intra*-grain heterogeneity. In contrast, the large particles (d > 35 nm) have comparatively minor *inter*-grain heterogeneity and significant *intra*-grain heterogeneity. Quantitatively, Figure 4b (i & iii) plots the profiles of ε_{002} of a selected grain along the path of particle center-to-edge: that for small particle of d = 30.1 nm exhibits steady increase in ε_{002} while that for large particle of d = 50.1 nm fluctuates and then increases toward the particle edge. Figure 4b (ii & iv) shows the profiles of ε_{002} along the particle boundaries, revealing significant dip near twin boundaries for the large particle although the profiles for each grain are similar, while the small particle shows a step-like pattern signaturing significant different values for two grains (from −1% to 2%). Figure S8 plots the histograms of the strain values of all the particles presented in Figure 4a. While the ensemble histograms of whole particles do not show an obvious dependence on particle size, those of each tetrahedral grain in a particle overlap more as the particle size increases, suggesting decreased inter-grain heterogeneity. Nevertheless, without the spatial information, it is much harder to notice the size trend, particularly the *intra*-grain heterogeneity.

2.4 | Particle Size-Dependent Spatial Distribution of Pseudosymmetry

Note that all the NPs on the ensemble level exhibit similar ranges of strain values; it is the spatial patterns of the strain values that show size-to-size, grain-to-grain, pixel-to-pixel variations, which can only be captured quantitatively and comprehensively by 4D-STEM. To understand and quantify the local lattice symmetry variation, we define and compute the k parameter, namely the *pseudosymmetry* parameter [16], the ratio of d-spacings along two lattice planes (d_{220}, d_{002}) based on the normal strain components and particle crystallography,

$$k = \frac{d_{220}}{d_{002}} = \frac{1}{\sqrt{2}}\left(\frac{1+\varepsilon_{220}}{1+\varepsilon_{002}}\right) = \tan\theta \tag{1}$$

where 2θ is the interplanar angle between the two (111) twinned directions when the Au lattice is at [110] zone axis (Figure 5a). In an ideal *fcc* lattice, 2θ is exactly 70.53°. For a fivefold twinned NP, it has been postulated that if all the five grains evenly divide 360°, 2θ must become 72° to close the gap, and this angular distortion is expected to break the symmetry from *fcc* through a tetragonal transformation into *bct* lattice (Figure 5a) [14]. This transformation can be measured by the k parameter (defined in Equation. (1) as a continuous description of the extent of symmetry breaking, ranging from no symmetry breaking (0.7071 for the bulk *fcc* lattice symmetry) to evenly dividing the space (0.7265 for *bct*).

As such, Figure 5b summarizes the k parameter maps of 16 particles with varied sizes. The trend starts with the observation of homogeneous distribution of *bct*-like symmetry across the entire particle for small NP size (row 1, Figure 5b; k map predominantly red). The dominance of *bct* lattice of the I4/mmm space group is consistent with recent literature of using X-ray diffraction to assign symmetry of highly monodispersed Au Dh NPs of similar sizes (31 and 49 nm therein) [17]. As the particle size increases further, *fcc*-like symmetry emerges, mostly within one grain, at the twin boundaries and edges (row 2, Figure 5b). Subsequently, at the particle level, k patterns appear more severely distorted (as darker red and black) while *fcc*-symmetry starts spreading to more than one grain (row 3, Figure 5b), corresponding to d ~ 35 nm crossover of inter-grain vs. intra-grain heterogeneity discussed in Figure 4. Lastly, *fcc*-like symmetry appears almost evenly near the five twin boundaries while the *bct*-symmetry regions stay within grains (row 4, Figure 5b), where inter-grain heterogeneity reduces with less distorted regions. Figure 5c plots the value distributions of k in each grain for the small particle at d = 20.5 nm and the large particle at d = 50.1 nm (Figure 5c).

15214095, 0, Downloaded from https://advanced.onlinelibrary.wiley.com/doi/10.1002/adma.202521638 by University Of Illinois At Urba, Wiley Online Library on [16/04/2026]. See the Terms and Conditions (https://onlinelibrary.wiley.com/terms-and-conditions) on Wiley Online Library for rules of use; OA articles are governed by the applicable Creative Commons License

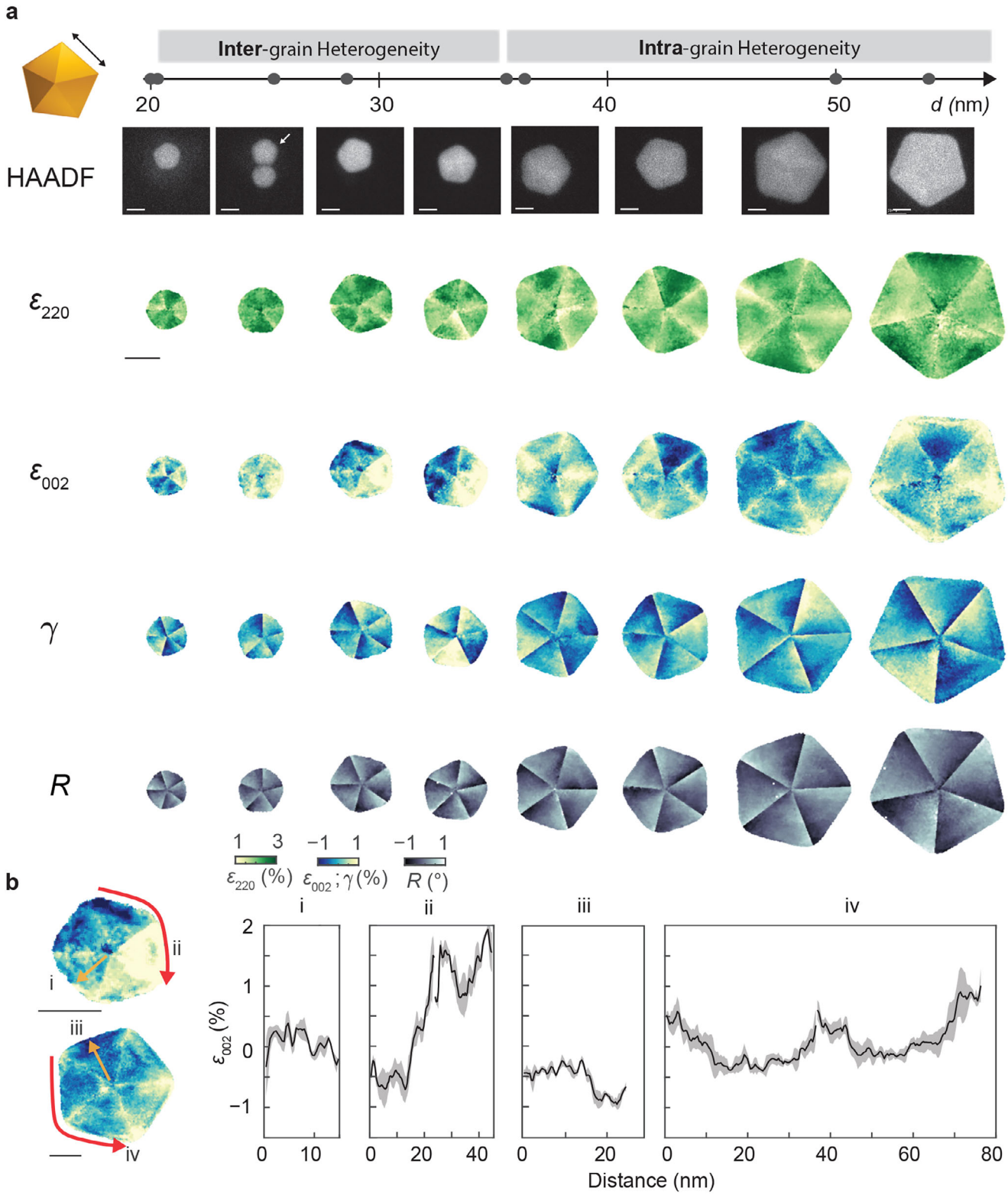

FIGURE 4 | Particle size dependence of strain distribution for each component and lattice rotation. (a) Particle morphologies shown by HAADF STEM images and strain maps of each strain component of particles of d between 20 and 55 nm. (b) Strain profiles of particle at d = 30.1 nm (i, ii) and d = 50.1 nm (iii, iv), calculated along the paths of center-to-edge as yellow arrows (i, iii) and around the NP edge as the red arrows (ii, iv). Scale bars: 20 nm.

15214095, 0, Downloaded from https://advanced.onlinelibrary.wiley.com/doi/10.1002/adma.202521658 by University Of Illinois At Urba, Wiley Online Library on [16/04/2026]. See the Terms and Conditions (https://onlinelibrary.wiley.com/terms-and-conditions) on Wiley Online Library for rules of use; OA articles are governed by the applicable Creative Commons License

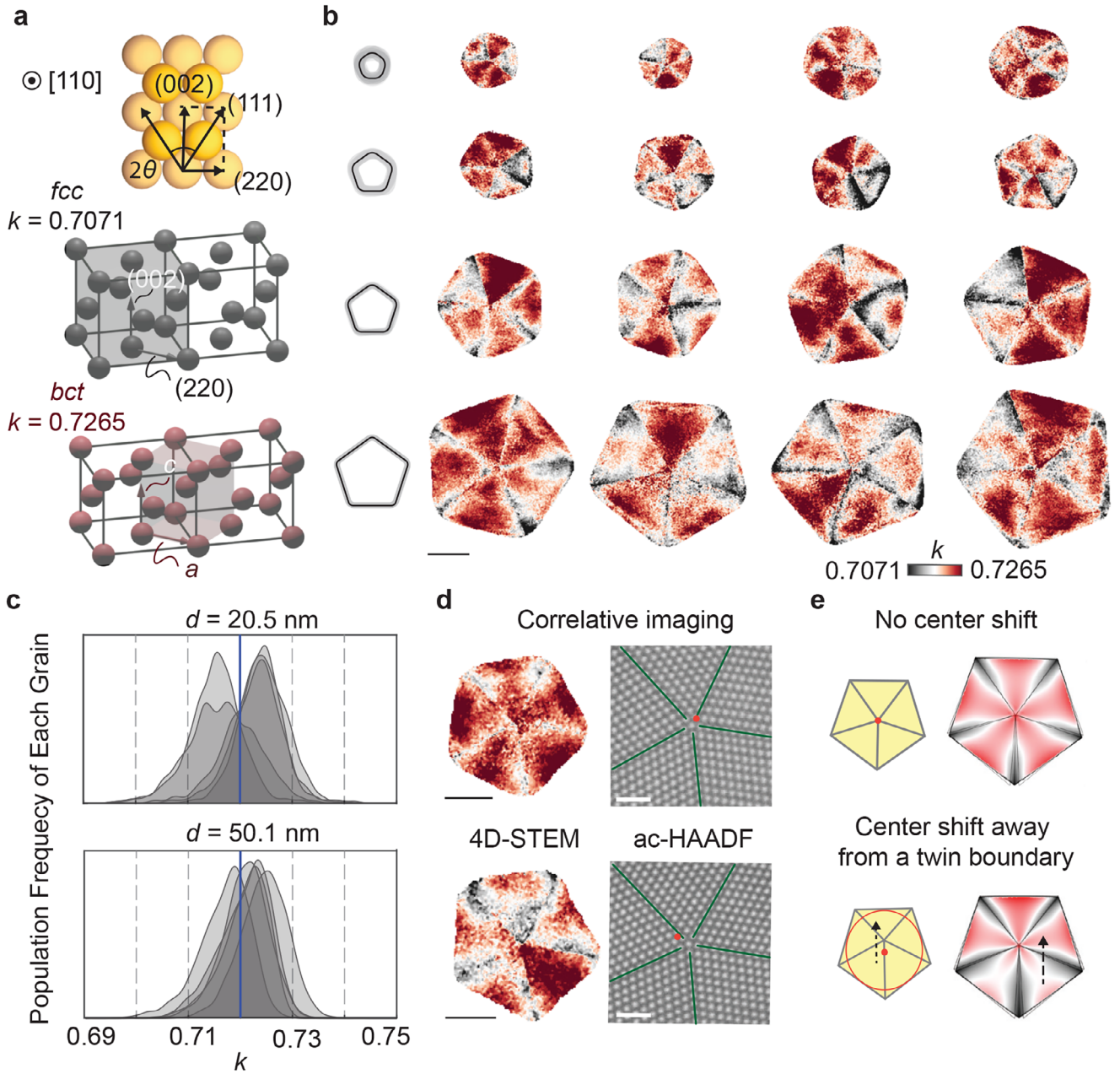

FIGURE 5 | Mapping of pseudosymmetry parameter of differently sized Dh particles. (a) Top: Au lattice model at (110) orientation with (002), (111), (220) lattice planes indicated and θ angle defined. Middle and bottom: schematics of symmetry transformation when the d-spacings of (002) and (220) lattice planes (in arrows) are strained unevenly, and how k is defined at two extreme cases. Each of their unit cells is shaded for visualization. (b) Lattice distortion maps of all particles. Inset on the left showing schematics of variation of particle morphology and tip truncation at each size range. (c) Histograms of population distribution of k in each grain of particles at $d = 20.5$ nm (top) and $d = 50.1$ nm (bottom). (d) Correlative imaging of two other particles at $d = 33.0$ nm (top) and $d = 34.1$ nm (bottom) using aberration corrected-STEM and 4D-STEM, showing the impact of particle center shifting on the map of lattice distortion. See magnified views in Figure S9. (e) FEA simulation results of k with no center shifting (top), center shifting away from the center along a twin boundary (bottom). Scale bars: 20 nm (4D-STEM mappings) and 1 nm (atomic HAADF images).

The distributions of the grains in small particle can be found to be centered around $k = 0.72$, which is the value each grain in the large particle homogenizes to. Wu et al. applied the same but modified analysis for atomic HAADF image of a small ($d < 10$ nm) particle, smaller than the particle size covered in our work, and found the averaged k across the entire particle to be 0.7168 (after conversion) [16]. The value closely coincides with our results measured by 4D-STEM herein, suggesting that the extent of symmetry breaking of the entire particle is size-independent; however, at the grain level, as particle size increases, the extent of inter-grain heterogeneity first increases and then decreases.

We reveal that the lattice pseudosymmetry of geometrically frustrated NPs spatially varies, and that its distribution is size-dependent. When referring to the strain maps, it can be observed that most of the *fcc*-regions have tensile strain in both normal directions. Furthermore, because shear strain is on the same

15214095, 0, Downloaded from https://advanced.onlinelibrary.wiley.com/doi/10.1002/adma.202521658 by University Of Illinois At Urba, Wiley Online Library on [16/04/2026]. See the Terms and Conditions (https://onlinelibrary.wiley.com/terms-and-conditions) on Wiley Online Library for rules of use; OA articles are governed by the applicable Creative Commons License

order of magnitude as the normal strain, the symmetry is distorted to base-centered monoclinic lattice symmetry, further highlighting the pseudosymmetric nature of Dh particles.

Correlative imaging of 4D-STEM-based pseudosymmetry parameter k map and atomic HAADF suggests the geometric origin of intra-grain heterogeneity. In Figure 5d, two particles at d = 33.0 nm (top) and 34.1 nm (bottom) show different mappings of lattice symmetry. The bottom particle shows one grain with significant lattice distortion and large intra-grain heterogeneity, while the top particle shows a more symmetrical distribution. From the HAADF images, we estimate the ideal positions of particle centers based on the particle shapes by inscribing a circle that approximates the NP shape as in theoretical models [57]. In the two particles, the ideal center (red dots, Figure 5d) of the bottom particle exhibits a larger shift from the experimentally observed center than that in the top particle. In FEA simulation, when we build models with the center shift and keep all other factors identical, the grain with distorted k can be reproduced (Figure 5e; Note S4). This comparison suggests that the feature of intra-grain heterogeneity is sensitive to the center shift of the disclination axis position. Physically, when the center shifts along the direction of one twin boundary, it increases the interplanar twin boundary angle (2θ) of the grains opposite to the shifting direction, leading to asymmetric distortion of the entire grain. Figure S9 shows that the five interplanar twin boundary angles for all grains qualitatively match the severity of lattice symmetry distortion in the grains, suggesting a correlation of intra-grain heterogeneity and the shifting of particle centers, which can also be related to NP shapes.

3 | Discussion

Although inter-grain heterogeneity has been observed as image contrast in TEM as early as 1987, further quantification has remained experimentally unexplored prior to our work [58]. Previous theoretical studies proposed "center-shifting," that is, disclination core displacement, as one of the defect mechanisms of disclination; others include additional twin boundaries, incoherent surface layers, etc [57]. Our work delineates a correlation between the center shifting and the internal structure of the entire particle. Regarding the energetic impact of this defect type, Ajayan and Marks theoretically showed that the energy cost of shifting the particle center can be modeled by a parabolic function of the amount of shifting from the additional surface energy for small particles (< 10 nm) [59, 60]. Yet, unlike these idealized models with circular particle shape and five twin boundaries distributed evenly at particle surfaces, our results show that, in realistic colloidal synthesis, particle geometry is more complex and impacts the strain distribution, local lattice distortion, and properties in geometrically frustrated systems.

For the particle size dependence of lattice straining at the nanoscale, we speculate the following reasons. First, when particles are small, grains spatially vary easily. Shape asymmetry factors such as center shifting contribute inter-grain heterogeneity (Figure 5d). Second, particles evolve from a rounded shape to faceted pentagonal bipyramids as NP size increases. As such, the nuance of facet-dependent surface energies starts to make a difference to modify the balance of volumetric strain energy with surface energy [61]. The Dh shape studied here only have dominated {111} facets. Similar particle size-dependent crossover can be different for Dh shapes with other facets (Marks, Ino Dh, or pentagonal rods, for example) [61–63]. Third, we observe that the quantitative transition of geometric gap closing behavior at d ~ 35 nm (Figure 2e) coincides with the qualitative crossover of heterogeneity of ε components at d ~ 35 nm (Figure 4) and the emergence of regions of *fcc*-like local lattice symmetry (Figure 5b). In other words, increasing particle size allows the strain and lattice distortion to redistribute and homogenize toward bulk behaviors.

The internal grain structure and overall particle morphology may be closely coupled. Interestingly, from HAADF image analysis on particle shapes, the standard deviations of five edge lengths and five tip truncations show that the shape also trends to be more symmetric and bulk-like among five grains at larger sizes (up to d = 70 nm shown in Figure S2). This trend implies the presence of a self-regulating mechanism among the growth rates at each grain. During particle growth, the highly under-coordinated atoms on the ridges of twin boundaries are the predominating nucleation sites for monomers from growth solution [64]. When particles have significant inter-grain heterogeneity, free surface energy landscapes of the two sides of the twin boundary ridge can be different for adatoms to diffuse and deposit. Prior studies have shown that surface strain can modulate the energy barriers associated with surface diffusion, thereby affecting growth kinetics [65], which is consistent with the appearance of dynamic diffraction contrasts (indication of local strain) observed in previous in situ liquid-phase TEM studies of Dh NP growth from seeds with diameters around 30 nm [66].

In colloidally synthesized NPs, the strain–diffusion coupling is further complicated by the presence of surface ligands. In the seed-mediated growth of Dh NPs studied here, the ligand not only stabilizes the particles in solution through its amphiphilic character but also promotes anisotropic growth of the {111} facets by preferential adsorption. Importantly, the strain state of the metal surface (compressive or tensile) can further regulate ligand adsorption. Tensile strain, for example, can increase the monomer diffusion barrier and simultaneously elevates the metal d-band center, thereby enhancing ligand binding and resulting in higher surface density [67]. From a total-energy perspective, highly strained regions require increased ligand coverage to compensate for the excess surface energy. This framework is consistent with our observation that grains along the direction of the particle center shifting are smaller and exhibit more severe pseudosymmetric distortion, correlating with reduced growth of those grains.

Perhaps the biggest surprise is how mechanically adaptive the Au lattice is, compared to other nanocrystalline metals such as Ag, Pd, and Cu, the latter of which show extended defects in fivefold twins to sustain the geometric frustration [32, 68, 69]. In other words, our workflow of mapping and understanding pseudosymmetry can extend to the multi-twinned NPs of different compositions. In Au Dh NPs, although local defects such as

15214095, 0, Downloaded from https://advanced.onlinelibrary.wiley.com/doi/10.1002/adma.202521638 by University Of Illinois At Urba, Wiley Online Library on [16/04/2026]. See the Terms and Conditions (https://onlinelibrary.wiley.com/terms-and-conditions) on Wiley Online Library for rules of use; OA articles are governed by the applicable Creative Commons License

vacancies may exist [70], they are unlikely to contribute to the long-range features of strain fields as significantly as extended defects (e.g., nanotwins, dislocation) [71]. Specifically, using the fivefold twins in Ag NPs as a comparison, which are more defect-prone, Au exhibits a distinctive set of bulk mechanical properties: doubled intrinsic stacking-fault energy (32 mJ/m^2 for Au vs. 16 mJ/m^2 for Ag), doubled twin-boundary energy (15 mJ/m^2 for Au vs. 8 mJ/m^2 for Ag), yet half the grain boundary energy (364 mJ/m^2 for Au vs 790 mJ/m^2 for Ag) [72]. These differences suggest mechanically, fivefold twinned structure of Au is more stable due to the low energy cost to generate twin boundary to accommodate the geometric frustration while preserving the Dh shape. These distinctions in mechanical properties help to explain previously reported studies on Ag Dh NP, where particle shapes can change when twin boundaries migrate to particle surfaces and create new facets [68].

Among the rapidly expanding library of colloidal synthesis strategies using particle shape, defects, alloying or shelling, and crystal structure to engineer lattice strain [73], Au Dh NPs represent one of the fundamental examples of geometric frustration at the nanoscale. Originated simply from the geometric mismatch of particle shape containing fivefold symmetry with the *fcc* atomic structure, the delicate energy balance among volume, surface, and strain energies emerges to distort the crystalline structure. Our work demonstrates that 4D-STEM resolves chemically meaningful structural information across an entire NP by aligning strain components with the major unit-cell axes of local lattices, thereby enhancing the interpretability of nanoscale mechanical responses. The pseudosymmetry–size correlation identified in this work provides new insight into the energy balance beyond the conventional characterization techniques. In this size range of 20–55 nm, these findings have direct implications for multi-twinned NPs used in catalysis [30, 31], plasmonics [36–38], and battery [40], where larger particles usually offer improved stability, better-defined geometry, and more materials volume although not necessarily higher catalytic activities, suggesting an intriguing balance for one to engineer NP size. More fundamentally, the concept of pseudosymmetry in multi-twinned NPs offers a new framework for understanding dynamic processes such as NP growth and gas adsorption [74, 75]. Note that during catalysis, NP surfaces and shape change due to heating-induced atomic migration or atomic displacement upon chemisorption of reactants or intermediates, and such change is ought to be governed by the (pseudo)symmetry and distortion modes of the underlying crystalline lattice. Thus in situ characterizations [76–79] coupled with the 4D-STEM mapping of the straining modes can be the next breakthrough in the field [50, 80].

Beyond shape-controlled colloidal synthesis, the pseudosymmetric mechanisms by which soft lattice accommodates symmetry breaking through shearing and twinning can be potentially generalized to the phase transformation in metallurgy, ceramics, and polymers [81–83]. For example, martensitic transformation is a fundamental process in metallurgy that undergoes *fcc* to *bcc*/*bct* phase transformation upon quenching the materials [84]. Though Bain distortion describes the homogeneous framework of pathways, it alone is insufficient to account for the observed crystallographic orientation relationships, which require consideration of additional lattice-invariant deformation pathways such as twinning or slip in polycrystalline materials [85]. Going beyond the single-component *fcc* Au NPs presented here, advanced processing of alloying can significantly alter the crystalline phase, such as the $L1_0$ phase in intermetallics of AuCu and FePt [43, 44]. In these cases, even when Dh shape and fivefold twins are maintained, the fundamental driving force for structural distortion, namely the geometric misfit, could change drastically from 7.35° to −13.35°, which will invite more future studies using the workflow that we demonstrate here. We envision that the method can be widely adaptable to metals or ceramics to not only study the fundamental pathways by local crystal structure with nm spatial resolution but also provide the opportunity to study interaction with local microstructure for mechanical and functional properties.

4 | Experimental Section

4.1 | Materials

Tetrachloroauric acid trihydrate ($HAuCl_4 \cdot 3H_2O$, ≥ 99.9% trace metal basis), hexadecyltrimethylammonium chloride (CTAC, 25 wt.% in H_2O), benzyldimethylhexadecylammonium chloride (BDAC, ≥ 97.0%), citric acid (CA, BioUltra, anhydrous, ≥ 99.5%), sodium borohydride ($NaBH_4$, ReagentPlus, ≥ 99.0%), L-ascorbic acid (AA, BioXtra, ≥ 99.0%) were all purchased from Sigma Aldrich, and used without further purification. Nanopure deionized (DI) water (18.2 MΩ·cm at 25°C) purified by the Milli-Q Advantage A10 system was used throughout the experiments.

4.2 | Synthesis of Gold Seeds

The synthesis of gold Dh NPs follows a previous method in the literature [9]. Gold seeds were prepared in a 20 mL scintillation vial under vigorous stirring at 1,200 rpm at room temperature. The solution was prepared by mixing 0.25 mL of 10 mM $HAuCl_4$, 0.50 mL of 100 mM CA, and 2.5 mL of 200 mM CTAC, all in aqueous solution, and an additional 6.75 mL of water to a final volume of 10 mL. Then, 0.25 mL of 25 mM $NaBH_4$ (freshly prepared with iced water) was added rapidly while maintaining stirring at 1,200 rpm, after which the vial was loosely capped to avoid immediate oxidation of $NaBH_4$. The solution immediately turned from yellow to brown, indicating the formation of Au clusters. After 2 min, the vial was tightly capped and transferred to an oil bath at 90°C for 90 min under gentle stirring (400 rpm). During this time, the color gradually changed from brown to red, suggesting the formation of Au seeds. Afterwards, the vial was taken out from oil bath, quenched to room temperature, and stored at ambient condition for subsequent growth. It is suggested that the seed solution should be used within one day, as delayed use may lead to slight truncation of the perfect Dh shape.

4.3 | Synthesis of gold Dh NPs

A desired volume of gold seed solution was added to a growth solution containing 0.1 mL of 50 mM $HAuCl_4$, 10 mL of 100 mM BDAC, and 0.075 mL of 100 mL AA under vigorous stirring at

15214095, 0, Downloaded from https://advanced.onlinelibrary.wiley.com/doi/10.1002/adma.202521658 by University Of Illinois At Urba, Wiley Online Library on [16/04/2026]. See the Terms and Conditions (https://onlinelibrary.wiley.com/terms-and-conditions) on Wiley Online Library for rules of use; OA articles are governed by the applicable Creative Commons License

30°C. Afterwards, the mixture was left undisturbed at 30°C for 30 min. The products were then collected by centrifugation at 8,000 rpm for 10 min. The sizes of Dh NP were controlled by the volume of gold seeds added: 500 μL for d = 20–30 nm NPs, 200 μL for d = 30–40 nm NPs, and 100 μL for d = 40–55 nm NPs.

4.4 | 4D-STEM Measurement

The TEM sample grid was prepared by drop-casting the NP solution. Specifically, gold Dh NP solutions were centrifuged at 5,000 rpm for 5 min twice, with water replacing the supernatant to remove excess ligands in between. A 5 μL droplet was then drop-casted onto TEM grid and let air dry. Before the imaging experiment, the grid was plasma cleaned (Tergo Plasma Cleaner, PIE Scientific) with argon and oxygen in immersion mode at 40 W of power for 2 min. In cases when excess ligands were present on the grid, they were to be further removed by dipping the grid into warm DI water (~ 40°C) for 10 s.

4D-STEM and HAADF imaging were performed in microprobe (μp) mode on a ThermoFisher Talos S/TEM with FEG-X gun operating at 200 kV. With 20 μm condenser (C2) aperture, gun lens 4–5, and spot size 7, the probe condition can repeatedly reproduce with convergence angle of 0.6 mrad, beam size of 2.0 nm at full-width-at-maximum (FWHM), and beam current of 7.4 pA (or 1.5×10^5 $e^{-}Å^{-2}s^{-1}$). The Dh NPs on the TEM grid were carefully tilt to the common [110] zone axis that all five grains share using a standard double-tilt holder before the raster scan of electron beam started. 4D-STEM datasets were collected on an Electron Microscope Pixelated Array Detector (EMPAD) at nominal camera length of 520 mm and nominal magnification of 1.05M× with the step size of 0.376 nm and exposure time of 1 ms. The HAADF images were collected by the same probe and imaging conditions using a HAADF detector with dwell time of 2–4 μs. All particles were maintained at the eucentric plane for a consistent sample-to-detector distance across particle for quantitative comparison. Each 4D-STEM dataset is 256 × 256 pixels, taking ~1 min to collect. 4D-STEM scans were performed at most twice for each particle.

4.5 | Correlative Measurement

Correlative measurement of 4D-STEM and aberration corrected-STEM imaging was performed on a ThermoFisher Themis Z S/TEM with FEG-X gun and aberration corrector operating at 300 kV. 4D-STEM was performed at μp mode with a gun lens of 783, spot size 9, and convergence angle of 0.461 mrad using a 50 μm C2 aperture at a nominal camera length of 1150 mm. The corresponding beam size is 1.7 nm at FWHM with a beam current of 17 pA. 4D-STEM datasets were collected on an EMPAD at a nominal camera length of 1150 mm, at a nominal magnification of 640k×, with a step size of 0.438 nm and an exposure time of 1 ms. Each 4D-STEM dataset is 256 × 256 pixels, taking ~1 min to collect. Correlatively, aberration corrected-STEM imaging was performed at nanoprobe (np) mode with gun lens of 783, spot size 9, convergence angle of 18 mrad using a 50 μm C2 aperture, and a beam current of 33 pA. The camera length was 115 mm with a collection angle range of 51–200 mrad for the HAADF detector with dwell time of 2–4 μs at a nominal magnification of 1.65 M× with the step size of 0.234 nm.

Author Contributions

O.L. and Q.C. conceived the project. Z.L. and S.M. synthesized the Au Dh NPs. O.L. and C.-Y.H. conducted the experiments. O.L., H.-C.N., X.W., C.-Y.H., and L.Y. developed and streamlined the data analysis. Y.J. performed the FEA simulations. Q.C. and J.-M.Z. supervised the work. O.L. and Q.C. wrote the manuscript. All authors discussed the results and contributed to the final manuscript.

Acknowledgements

This research is based upon work supported by the U.S. Department of Energy, Office of Science, Office of Basic Energy Sciences, under Award Number DE-SC0024064. Experiments were carried out in part in the Materials Research Laboratory, Central Research Facilities, University of Illinois.

Conflicts of Interest

The authors declare no conflicts of interest.

Data Availability Statement

The data that support the findings of this study are available from the corresponding authors on request. The raw 4D-STEM datasets of the 26 particles listed in Table S1 can be found at https://doi.org/10.13012/B2IDB-3832353_V1. The custom data processing codes in MATLAB and Python (in Jupyter Notebook form) used in this study are available from GitHub (https://github.com/chenlabUIUC/Decahedral-strain-mapping).

References

1. K. Zhao, H. Deng, H. Chen, et al., "Realization of the Kagome Spin Ice state in a Frustrated Intermetallic Compound," *Science* 367 (2020): 1218–1223, https://doi.org/10.1126/science.aaw1666.

2. K. Liu, P. P. Pratapa, D. Misseroni, T. Tachi, and G. H. Paulino, "Triclinic Metamaterials by Tristable Origami With Reprogrammable Frustration," *Advanced Materials* 34 (2022): 2107998, https://doi.org/10.1002/adma.202107998.

3. D. L. D. Caspar and A. Klug, "Physical Principles in the Construction of Regular Viruses," *Cold Spring Harbor Symposia on Quantitative Biology* 27 (1962): 1–24, https://doi.org/10.1101/SQB.1962.027.001.005.

4. D. S. Goodsell and A. J. Olson, "Structural Symmetry and Protein Function," *Annual Review of Biophysics and Biomolecular Structure* 29 (2000): 105–153, https://doi.org/10.1146/annurev.biophys.29.1.105.

5. P. M. Colman, W. G. Laver, J. N. Varghese, et al., "Three-Dimensional Structure of a Complex of Antibody With Influenza Virus Neuraminidase," *Nature* 326 (1987): 358–363, https://doi.org/10.1038/326358a0.

6. B. G. Bagley, "A Dense Packing of Hard Spheres With Five-Fold Symmetry," *Nature* 208 (1965): 674–675, https://doi.org/10.1038/208674a0.

7. Y. Xia, Y. Xiong, B. Lim, and S. E. Skrabalak, "Shape-Controlled Synthesis of Metal Nanocrystals: Simple Chemistry Meets Complex Physics?," *Angewandte Chemie International Edition* 48 (2009): 60–103, https://doi.org/10.1002/anie.200802248.

8. H. Hofmeister, "Shape Variations and Anisotropic Growth of Multiply Twinned Nanoparticles," *Zeitschrift für Kristallographie* 224 (2009): 528–538, https://doi.org/10.1524/zkri.2009.1034.

9. A. Sánchez-Iglesias, N. Winckelmans, T. Altantzis, S. Bals, M. Grzelczak, and L. M. Liz-Marzán, "High-Yield Seeded Growth of Monodisperse Pentatwinned Gold Nanoparticles Through Thermally

15214095, 0, Downloaded from https://advanced.onlinelibrary.wiley.com/doi/10.1002/adma.202521638 by University Of Illinois At Urba, Wiley Online Library on [16/04/2026]. See the Terms and Conditions (https://onlinelibrary.wiley.com/terms-and-conditions) on Wiley Online Library for rules of use; OA articles are governed by the applicable Creative Commons License

Induced Seed Twinning," *Journal of the American Chemical Society* 139 (2017): 107–110, https://doi.org/10.1021/jacs.6b12143.

10. J. Rodríguez-Fernández, C. Novo, V. Myroshnychenko, et al., "Spectroscopy, Imaging, and Modeling of Individual Gold Decahedra," *The Journal of Physical Chemistry C* 113 (2009): 18623–18631, https://doi.org/10.1021/jp907646d.

11. J. Wu, L. Qi, H. You, A. Gross, J. Li, and H. Yang, "Icosahedral Platinum Alloy Nanocrystals With Enhanced Electrocatalytic Activities," *Journal of the American Chemical Society* 134 (2012): 11880–11883, https://doi.org/10.1021/ja303950v.

12. R. He, Y.-C. Wang, X. Wang, et al., "Facile Synthesis of Pentacle Gold–copper Alloy Nanocrystals and Their Plasmonic and Catalytic Properties," *Nature Communications* 5 (2014): 4327.

13. X. Sun, L. Sun, L. Lin, et al., "Tuning the Geometry and Optical Chirality of Pentatwinned Au Nanoparticles With 5-Fold Rotational Symmetry," *ACS Nano* 18 (2024): 9543–9556, https://doi.org/10.1021/acsnano.3c12637.

14. C. Y. Yang, "Crystallography of decahedral and icosahedral particles," *Journal of Crystal Growth* 47 (1979): 274–282, https://doi.org/10.1016/0022-0248(79)90252-5.

15. J. Diao, K. Gall, and M. L. Dunn, "Surface-Stress-Induced Phase Transformation in Metal Nanowires," *Nature Materials* 2 (2003): 656–660, https://doi.org/10.1038/nmat977.

16. H. Wu, R. Yu, J. Zhu, W. Chen, Y. Li, and T. Wang, "Size-Dependent Strain in Fivefold Twins of Gold," *Acta Crystallographica Section B Structural Science, Crystal Engineering and Materials* 77 (2021): 93–98, https://doi.org/10.1107/S2052520620014791.

17. C. Martín-Sánchez, A. Sánchez-Iglesias, J. A. Barreda-Argüeso, et al., "Origin of the Rich Polymorphism of Gold in Penta-Twinned Nanoparticles," *Nano Letters* 25 (2025): 3588–3596, https://doi.org/10.1021/acs.nanolett.4c06473.

18. S. Choi, J. A. Herron, J. Scaranto, et al., "A Comprehensive Study of Formic Acid Oxidation on Palladium Nanocrystals With Different Types of Facets and Twin Defects," *Chemcatchem* 7 (2015): 2077–2084, https://doi.org/10.1002/cctc.201500094.

19. J. A. R. Clarke and J. D. Bernal, "A Dense Packing of Hard Spheres With Five-Fold Symmetry," *Nature* 211 (1966): 280, https://doi.org/10.1038/211280a0.

20. A. Howie and L. D. Marks, "Elastic Strains and the Energy Balance for Multiply Twinned Particles," *Philosophical Magazine A* 49 (1984): 95–109.

21. E. Roduner, "Size Matters: Why Nanomaterials Are Different," *Chemical Society Reviews* 35 (2006): 583, https://doi.org/10.1039/b502142c.

22. K. A. Fichthorn, "Theory of Anisotropic Metal Nanostructures," *Chemical Reviews* 123 (2023): 4146–4183, https://doi.org/10.1021/acs.chemrev.2c00831.

23. Y. Sun, Y. Ren, Y. Liu, J. Wen, J. S. Okasinski, and D. J. Miller, "Ambient-Stable Tetragonal Phase in Silver Nanostructures," *Nature Communications* 3 (2012): 6–11, https://doi.org/10.1038/ncomms1963.

24. W. Ji, W. Qi, X. Li, et al., "Investigation of Disclinations in Marks Decahedral Pd Nanoparticles by Aberration-Corrected HRTEM," *Materials Letters* 152 (2015): 283–286, https://doi.org/10.1016/j.matlet.2015.03.137.

25. Z. Li, Z. Xie, Y. Zhang, et al., "Probing the Atomically Diffuse Interfaces in Pd@Pt Core-Shell Nanoparticles in Three Dimensions," *Nature Communications* 14 (2023): 2934, https://doi.org/10.1038/s41467-023-38536-z.

26. A. Mayoral, H. Barron, R. Estrada-Salas, A. Vazquez-Duran, and M. José-Yacamán, "Nanoparticle Stability From the Nano to the Meso Interval," *Nanoscale* 2 (2010): 335–342, https://doi.org/10.1039/B9NR00287A.

27. B. Rogers, A. Lehr, J. J. Velázquez-Salazar, et al., "Decahedra and Icosahedra Everywhere: The Anomalous Crystallization of Au and Other Metals at the Nanoscale," *Crystal Research and Technology* 58 (2023): 2200256–2200259, https://doi.org/10.1002/crat.202200259.

28. W. Chen, X. Zhan, R. Yuan, et al., "Formation and Impact of Nanoscopic Oriented Phase Domains in Electrochemical Crystalline Electrodes," *Nature Materials* 22 (2023): 92–99, https://doi.org/10.1038/s41563-022-01381-4.

29. M. Song, G. Zhou, N. Lu, et al., "Oriented Attachment Induces Fivefold Twins by Forming and Decomposing High-Energy Grain Boundaries," *Science* 367 (2020): 40–45, https://doi.org/10.1126/science.aax6511.

30. A. Loiudice, P. Lobaccaro, E. A. Kamali, et al., "Tailoring Copper Nanocrystals Towards C_2 Products in Electrochemical CO_2 Reduction," *Angewandte Chemie, International Edition* 55 (2016): 5789–5792.

31. R. Reske, H. Mistry, F. Behafarid, B. Roldan Cuenya, and P. Strasser, "Particle Size Effects in the Catalytic Electroreduction of CO_2 on Cu Nanoparticles," *Journal of the American Chemical Society* 136 (2014): 6978–6986.

32. C. Choi, T. Cheng, M. Flores Espinosa, et al., "A Highly Active Star Decahedron Cu Nanocatalyst for Hydrocarbon Production at Low Overpotentials," *Advanced Materials* 31 (2019): 1805405, https://doi.org/10.1002/adma.201805405.

33. J. Kim, X. Song, F. Ji, et al., "Polymorphic Assembly From Beveled Gold Triangular Nanoprisms," *Nano Letters* 17 (2017): 3270–3275, https://doi.org/10.1021/acs.nanolett.7b00958.

34. A. Kim, T. Vo, H. An, et al., "Symmetry-Breaking in Patch Formation on Triangular Gold Nanoparticles by Asymmetric Polymer Grafting," *Nature Communications* 13 (2022): 6774, https://doi.org/10.1038/s41467-022-34246-0.

35. S. Zhou, J. Li, J. Lu, et al., "Chiral Assemblies of Pinwheel Superlattices on Substrates," *Nature* 612 (2022): 259–265, https://doi.org/10.1038/s41586-022-05384-8.

36. I. Pastoriza-Santos, A. Sánchez-Iglesias, F. J. García de Abajo, and L. M. Liz-Marzán, "Environmental Optical Sensitivity of Gold Nanodecahedra," *Advanced Functional Materials* 17 (2007): 1443–1450, https://doi.org/10.1002/adfm.200601071.

37. H. Chen, X. Kou, Z. Yang, W. Ni, and J. Wang, "Shape- and Size-Dependent Refractive Index Sensitivity of Gold Nanoparticles," *Langmuir* 24 (2008): 5233–5237, https://doi.org/10.1021/la800305j.

38. K. G. Stamplecoskie, J. C. Scaiano, V. S. Tiwari, and H. Anis, "Optimal Size of Silver Nanoparticles for Surface-Enhanced Raman Spectroscopy," *The Journal of Physical Chemistry C* 115 (2011): 1403–1409, https://doi.org/10.1021/jp106666t.

39. Z. Tang, W. Chen, Z. Lyu, and Q. Chen, "Size-Dependent Reaction Mechanism of λ -MnO_2 Particles as Cathodes in Aqueous Zinc-Ion Batteries," *Energy Material Advances* 2022 (2022): 9765710.

40. W. Chen, X. Zhan, B. Luo, et al., "Effects of Particle Size on Mg^{2+} Ion Intercalation Into λ-MnO_2 Cathode Materials," *Nano Letters* 19 (2019): 4712–4720, https://doi.org/10.1021/acs.nanolett.9b01780.

41. M. Wagemaker, F. M. Mulder, and A. Van Der Ven, "The Role of Surface and Interface Energy on Phase Stability of Nanosized Insertion Compounds," *Advanced Materials* 21 (2009): 2703–2709, https://doi.org/10.1002/adma.200803038.

42. A. Van Der Ven, K. Garikipati, S. Kim, and M. Wagemaker, "The Role of Coherency Strains on Phase Stability in Li_xFePO_4: Needle Crystallites Minimize Coherency Strain and Overpotential," *Journal of the Electrochemical Society* 156 (2009): A949.

43. Z.-A. Li, M. Spasova, Q. M. Ramasse, M. E. Gruner, C. Kisielowski, and M. Farle, "Chemically Ordered Decahedral FePt Nanocrystals Observed by Electron Microscopy," *Physical Review B* 89 (2014): 161406, https://doi.org/10.1103/PhysRevB.89.161406.

44. C. Liang and Y. Yu, "Understanding the Formation of Multiply Twinned Structure in Decahedral Intermetallic Nanoparticles," *IUCrJ* 6 (2019): 447–453, https://doi.org/10.1107/S2052252519002562.

45. D. Dorignac, S. Delclos, and F. Phillipp, "Atomic Structure of a Complex Defect Configuration in Synthetic Diamond: A Fivefold Twin Centre

15214095, 0, Downloaded from https://advanced.onlinelibrary.wiley.com/doi/10.1002/adma.202521638 by University Of Illinois At Urba, Wiley Online Library on [16/04/2026]. See the Terms and Conditions (https://onlinelibrary.wiley.com/terms-and-conditions) on Wiley Online Library for rules of use; OA articles are governed by the applicable Creative Commons License

Connected to Two High-Order Grain Boundaries," *Philosophical Magazine B* 81 (2001): 1879–1891, https://doi.org/10.1080/13642810108223124.

46. S. Zhou, M. Zhao, T. H. Yang, and Y. Xia, "Decahedral Nanocrystals of Noble Metals: Synthesis, Characterization, and Applications," *Materials Today* 22 (2019): 108–131.

47. T. Zhang, X. Li, Y. Sun, et al., "A Universal Route With Fine Kinetic Control to a family of Penta-Twinned Gold Nanocrystals," *Chemical Science* 12 (2021): 12631–12639, https://doi.org/10.1039/D1SC03040J.

48. R. Yuan, J. Zhang, and J.-M. Zuo, "Lattice Strain Mapping Using Circular Hough Transform for Electron Diffraction Disk Detection," *Ultramicroscopy* 207 (2019): 112837, https://doi.org/10.1016/j.ultramic.2019.112837.

49. S. Kang, D. Wang, C. Kübel, and X. Mu, "Importance of TEM Sample Thickness for Measuring Strain Fields," *Ultramicroscopy* 255 (2024): 113844, https://doi.org/10.1016/j.ultramic.2023.113844.

50. C. Liu, O. Lin, S. Pidaparthy, et al., "4D-STEM Mapping of Nanocrystal Reaction Dynamics and Heterogeneity in a Graphene Liquid Cell," *Nano Letters* 24 (2024): 3890–3897, https://doi.org/10.1021/acs.nanolett.3c05015.

51. Z. Lyu, L. Yao, W. Chen, F. C. Kalutantirige, and Q. Chen, "Electron Microscopy Studies of Soft Nanomaterials," *Chemical Reviews* 123 (2023): 4051–4145, https://doi.org/10.1021/acs.chemrev.2c00461.

52. G. Yan, G. Kim, R. Yuan, et al., "The Role of Solid Solutions in Iron Phosphate-Based Electrodes for Selective Electrochemical Lithium Extraction," *Nature Communications* 13 (2022): 4579, https://doi.org/10.1038/s41467-022-32369-y.

53. C. L. Johnson, E. Snoeck, M. Ezcurdia, et al., "Effects of Elastic Anisotropy on Strain Distributions in Decahedral Gold Nanoparticles," *Nature Materials* 7 (2008): 120–124, https://doi.org/10.1038/nmat2083.

54. B. Goris, J. De Beenhouwer, A. De Backer, et al., "Measuring Lattice Strain in Three Dimensions Through Electron Microscopy," *Nano Letters* 15 (2015): 6996–7001, https://doi.org/10.1021/acs.nanolett.5b03008.

55. J. S. Du, W. Zhou, S. M. Rupich, and C. A. Mirkin, "Twin Pathways: Discerning the Origins of Multiply Twinned Colloidal Nanoparticles," *Angewandte Chemie International Edition* 60 (2021): 6858–6863, https://doi.org/10.1002/anie.202015166.

56. M. Raffel, C. E. Willert, and J. Kompenhans, *Particle Image Velocimetry: A Practical Guide* (Springer-Verlag, 1998), https://doi.org/10.1007/978-3-662-03637-2.

57. V. G. Gryaznov, J. Heydenreich, A. M. Kaprelov, S. A. Nepijko, A. E. Romanov, and J. Urban, "Pentagonal Symmetry and Disclinations in Small Particles," *Crystal Research and Technology* 34 (1999): 1091–1119, https://doi.org/10.1002/(SICI)1521-4079(199911)34:9%3c1091::AID-CRAT1091%3e3.0.CO;2-S.

58. S. Iijima, "Fine Particles of Silicon. I. Crystal Growth of Spherical Particles of Si," *Japanese Journal of Applied Physics* 26 (1987): 357, https://doi.org/10.1143/JJAP.26.357.

59. P. M. Ajayan and L. D. Marks, "Quasimelting and Phases of Small Particles," *Physical Review Letters* 60 (1988): 585–587, https://doi.org/10.1103/PhysRevLett.60.585.

60. L. D. Marks and L. Peng, "Nanoparticle Shape, Thermodynamics and Kinetics," *Journal of Physics: Condensed Matter* 28 (2016): 053001.

61. E. Ringe, R. P. Van Duyne, and L. D. Marks, "Kinetic and Thermodynamic Modified Wulff Constructions for Twinned Nanoparticles," *The Journal of Physical Chemistry C* 117 (2013): 15859–15870, https://doi.org/10.1021/jp401566m.

62. Z. Cheng, C. Shi, K. Zhao, M. Engel, M. R. Jones, and Y. Han, "Precision Mapping of Equilibrium Disclination Strain in Pentagonally Twinned Nanostructures," *Science Advances* 11 (2025): aea9781, https://doi.org/10.1126/sciadv.aea9781.

63. S. Patala, L. D. Marks, M. O. De, and L. Cruz, "Elastic Strain Energy Effects in Faceted Decahedral Nanoparticles," *The Journal of Physical Chemistry C* 117 (2013): 1485–1494, https://doi.org/10.1021/jp310045g.

64. X. Wang, M. Vara, M. Luo, et al., "Pd@Pt Core–Shell Concave Decahedra: A Class of Catalysts for the Oxygen Reduction Reaction With Enhanced Activity and Durability," *Journal of the American Chemical Society* 137 (2015): 15036–15042.

65. H. Brune, K. Bromann, H. Röder, et al., "Effect of Strain on Surface Diffusion and Nucleation," *Physical Review B* 52 (1995): R14380–R14383, https://doi.org/10.1103/PhysRevB.52.R14380.

66. X. Ma, F. Lin, X. Chen, and C. Jin, "Unveiling Growth Pathways of Multiply Twinned Gold Nanoparticles by in Situ Liquid Cell Transmission Electron Microscopy," *ACS Nano* 14 (2020): 9594–9604, https://doi.org/10.1021/acsnano.9b10173.

67. T. Adit Maark and A. A. Peterson, "Understanding Strain and Ligand Effects in Hydrogen Evolution Over Pd(111) Surfaces," *The Journal of Physical Chemistry C* 118 (2014): 4275–4281, https://doi.org/10.1021/jp4121035.

68. M. Song, Z. Wu, N. Lu, and D. Li, "Strain Relaxation-Induced Twin Interface Migration and Morphology Evolution of Silver Nanoparticles," *Chemistry of Materials* 31 (2019): 842–850, https://doi.org/10.1021/acs.chemmater.8b03984.

69. W. Ji, W. Qi, S. Tang, et al., "Synthesis of Marks-Decahedral Pd Nanoparticles in Aqueous Solutions," *Particle & Particle Systems Characterization* 31 (2014): 851–856, https://doi.org/10.1002/ppsc.201400003.

70. C.-C. Chen, C. Zhu, E. R. White, et al., "Three-Dimensional Imaging of Dislocations in a Nanoparticle at Atomic Resolution," *Nature* 496 (2013): 74–77, https://doi.org/10.1038/nature12009.

71. Q. Yu, L. Qi, K. Chen, R. K. Mishra, J. Li, and A. M. Minor, "The Nanostructured Origin of Deformation Twinning," *Nano Letters* 12 (2012): 887–892, https://doi.org/10.1021/nl203937t.

72. J. P. Hirth and J. Lothe, Theory of Dislocation, Krieger (Reprint), Originally Published By Wiley, Malabar, Florida (for Krieger), Originally New York (Wiley), (1991).

73. M. H. Oh, M. G. Cho, D. Y. Chung, et al., "Design and Synthesis of Multigrain Nanocrystals via Geometric Misfit Strain," *Nature* 577 (2020): 359–363, https://doi.org/10.1038/s41586-019-1899-3.

74. J. Cui, S. Phul, and K. A. Fichthorn, "Diffusion Growth Mechanism of Penta-Twinned Ag Nanocrystals From Decahedral Seeds," *The Journal of Chemical Physics* 158 (2023): 164707, https://doi.org/10.1063/5.0146305.

75. A. F. Suzana, A. Rochet, A. R. Passos, et al., "In Situ Three-Dimensional Imaging of Strain in Gold Nanocrystals During Catalytic Oxidation," *Nanoscale Advances* 1 (2019): 3009–3014, https://doi.org/10.1039/C9NA00231F.

76. Q. Chen, J. M. Yuk, M. R. Hauwiller, et al., "Nucleation, Growth, and Superlattice Formation of Nanocrystals Observed in Liquid Cell Transmission Electron Microscopy," *MRS Bulletin* 45 (2020): 713–726, https://doi.org/10.1557/mrs.2020.229.

77. Z. Ou, L. Yao, H. An, B. Shen, and Q. Chen, "Imaging How Thermal Capillary Waves and Anisotropic Interfacial Stiffness Shape Nanoparticle Supracrystals," *Nature Communications* 11 (2020): 4555, https://doi.org/10.1038/s41467-020-18363-2.

78. B. Luo, Z. Wang, T. Curk, et al., "Unravelling Crystal Growth of Nanoparticles," *Nature Nanotechnology* 18 (2023): 589–595, https://doi.org/10.1038/s41565-023-01355-w.

79. C. Qian, E. Stanifer, Z. Ma, et al., "Nanoscale Phonon Dynamics in Self-Assembled Nanoparticle Lattices," *Nature Materials* 24 (2025): 1616–1625, https://doi.org/10.1038/s41563-025-02253-3.

80. M. Perxés Perich, J.-W. Lankman, C. J. Keijzer, and J. E. S. Van Der Hoeven, "*In Situ* Gas-Phase 4D-STEM for Strain Mapping during Hydride Formation in Palladium Nanocubes," *Nano Letter* 25 (2025): 5444–5451.

15214095, 0, Downloaded from https://advanced.onlinelibrary.wiley.com/doi/10.1002/adma.202521658 by University Of Illinois At Urba, Wiley Online Library on [16/04/2026]. See the Terms and Conditions (https://onlinelibrary.wiley.com/terms-and-conditions) on Wiley Online Library for rules of use; OA articles are governed by the applicable Creative Commons License

81. Y. Zhang, J. Cui, K.-Y. Chen, et al., "A Smart Coating With Integrated Physical Antimicrobial and Strain-Mapping Functionalities for Orthopedic Implants," *Science Advances* 9 (2023): adg7397, https://doi.org/10.1126/sciadv.adg7397.

82. A. Khasbaatar, A. Cheng, A. L. Jones, et al., "Solution Aggregate Structures of Donor Polymers Determine the Morphology and Processing Resiliency of Non-Fullerene Organic Solar Cells," *Chemistry of Materials* 35 (2023): 2713–2729, https://doi.org/10.1021/acs.chemmater.2c02141.

83. K. S. Park, Z. Xue, B. B. Patel, et al., "Chiral Emergence in Multistep Hierarchical Assembly of Achiral Conjugated Polymers," *Nature Communications* 13 (2022): 2738, https://doi.org/10.1038/s41467-022-30420-6.

84. M. Ahlers, "The Martensitic Transformation: Mechanisms and Crystallography," *Philosophical Magazine A* 82 (2002): 1093–1114, https://doi.org/10.1080/01418610208240019.

85. L. Sandoval, H. M. Urbassek, and P. Entel, "The Bain versus Nishiyama–Wassermann Path in the Martensitic Transformation of Fe," *New Journal of Physics* 11 (2009): 103027.

Supporting Information

Additional supporting information can be found online in the Supporting Information section.

Supporting File: adma73028-sup-0001-SuppMat.pdf.

15214095, 0, Downloaded from https://advanced.onlinelibrary.wiley.com/doi/10.1002/adma.202521658 by University Of Illinois At Urba, Wiley Online Library on [16/04/2026]. See the Terms and Conditions (https://onlinelibrary.wiley.com/terms-and-conditions) on Wiley Online Library for rules of use; OA articles are governed by the applicable Creative Commons License